

# Constraining the Mass Distribution of Cluster Galaxies by Weak Lensing

Bernhard Geiger<sup>1,2</sup> and Peter Schneider<sup>1</sup>

<sup>1</sup>Max-Planck-Institut für Astrophysik, Karl-Schwarzschild-Straße 1, 85740 Garching bei München, Germany

<sup>2</sup>Institut d’Astrophysique de Paris, 98bis Boulevard Arago, 75014 Paris, France

Accepted . Received

## ABSTRACT

Analysing the weak lensing distortions of the images of faint background galaxies provides a means to constrain the average mass distribution of cluster galaxies and potentially to test the extent of their dark matter haloes as a function of the density of their environment. The observable image distortions are a consequence of the interplay between the effects of a global cluster mass distribution and the perturbations due to individual cluster galaxies. Starting from a reconstruction of the cluster mass distribution with conventional techniques, we apply a maximum likelihood method to infer the average properties of an ensemble of cluster galaxies. From simulations this approach is found to be reliable as long as the galaxies including their dark matter haloes only contribute a small fraction to the total mass of the system. If their haloes are extended, the galaxies contain a substantial mass fraction. In this case our method is still applicable in the outer regions of clusters, where the surface mass density is low, but yields biased estimates of the parameters describing the mass profiles of the cluster galaxies in the central part of the cluster. In that case it will be necessary to resort to more sophisticated strategies by modelling cluster galaxies and an underlying global mass distribution simultaneously. We conclude that galaxy-galaxy lensing in clusters provides a unique means to probe the presence and extent of dark haloes of cluster galaxies.

**Key words:** gravitational lensing – galaxies: haloes – galaxies: clusters: general – dark matter

## 1 INTRODUCTION

Measurements of the rotation curves of spiral galaxies indicate that they are embedded in massive dark matter haloes. Although less straightforward, similar kinematical studies for elliptical galaxies point in the same direction, and are reinforced by a quantitative statistical analysis of surveys of gravitationally lensed QSOs (Maoz & Rix 1993). The deflection of light rays through the gravitational action of mass concentrations, usually called gravitational lensing, provides a way to obtain information about the mass distribution of galaxies at large radial distances from their centre. [At such distances, the only luminous test particles to investigate the gravitational potential are satellite galaxies with which the haloes of (field) galaxies can be probed to  $\sim 200$ kpc radius (Zaritsky & White 1994, Zaritsky et al. 1997).] The light deflection causes small distortions of the images of faint background galaxies. Recent statistical analyses (Brainerd, Blandford & Smail 1996, Griffiths et al. 1996) of these weak distortion effects suggest that the dark haloes of (field) galaxies are indeed fairly extended, as some popular theories

of structure formation predict them to be. During the formation of galaxy clusters the extended haloes of galaxies may be stripped off due to tidal forces of the cluster potential or during encounters with other galaxies. Ultimately the individual galaxy haloes should merge and form a global cluster halo. In this paper we discuss how this merging picture could be tested observationally by exploiting weak lensing effects.

The distortions of the images of background galaxies produced by massive galaxy clusters are strong enough to allow a parameter-free reconstruction of the clusters’ surface mass density. In the last few years several algorithms of this kind have been developed (e.g., Kaiser & Squires 1993, Seitz & Schneider 1995, 1996, Bartelmann et al. 1996, Squires & Kaiser 1996) and successfully applied (e.g., Fahlman et al. 1994, Squires et al. 1996, Seitz et al. 1996, Fischer et al. 1997). The smoothing length which has to be implemented in these techniques, however, is larger than galaxy scales, and the amount of information available does not suffice to reconstruct cluster galaxies individually. Therefore, one has to superpose the effects of a large number of galaxies statistically in order to infer the average properties of an ensemble

of galaxies. In clusters the advantages – compared to ‘galaxy-galaxy lensing’ studies in the field – are the larger number density of lens galaxies and the general amplification of their lensing effects caused by the underlying cluster mass distribution. However, the analysis is significantly more difficult technically, because it is necessary to disentangle the contribution to the image distortions due to individual cluster galaxies from those of the global cluster mass distribution.

In Section 2 we present simulations of a galaxy cluster, which are sufficiently realistic for the purposes of this work, and discuss how individual galaxies modify the distortion pattern of a smooth cluster mass distribution. In Section 3 we investigate the applicability of the so-called  $\zeta$ -statistic for obtaining information about the cluster galaxies. Section 4 represents the main part of this paper. Here we describe a maximum likelihood method for constraining the mass distribution of cluster galaxies, which is based on a reconstruction of the cluster mass distribution according to the methods mentioned above. Finally, the results are summarized in Section 5.

Recently, the weak lensing effects induced by cluster galaxies were also discussed by Natarajan & Kneib (1997). We will comment below on some of the differences between their approach and ours.

## 2 SIMULATIONS

### 2.1 Cluster and Cluster Galaxies

We selected a galaxy cluster located at a redshift  $z_d = 0.16$  from numerical cold-dark-matter simulations (Bartelmann, Steinmetz & Weiss 1995). In order to produce a map of the surface mass density  $\Sigma$  from the positions of the N-body particles, a smoothing procedure on scales of about  $15''$  was employed. We consider a square field of view with a side length of  $10'$ , which corresponds to a physical size of  $1.08h^{-1}$  Mpc at the cluster redshift ( $\Omega = 1$ ,  $\Lambda = 0$ , and  $H_0 = 100h \text{ km s}^{-1} \text{Mpc}^{-1}$ ). The total mass within that region is  $5.4 \times 10^{14}h^{-1} \text{ M}_\odot$ .

For lensing purposes it is convenient to express the surface mass density in dimensionless form as

$$\kappa = \frac{\Sigma}{\Sigma_{\text{crit}}} \quad \text{with} \quad \Sigma_{\text{crit}} = \frac{c^2}{4\pi G} \frac{D_s}{D_d D_{\text{ds}}}. \quad (1)$$

Here  $D_s$ ,  $D_d$ , and  $D_{\text{ds}}$  are the angular diameter distances from the observer to the lensed sources, from the observer to the lensing mass distribution, and between the lens and the sources, respectively. Locally, the lensing properties are specified by the dimensionless surface mass density  $\kappa$  and the shear  $\gamma$ , which are combinations of second order derivatives of a common two-dimensional scalar deflection potential. The shear is a dimensionless two-component quantity, regarded as a complex number in this paper, and can be computed by integrating over the surface mass distribution with an appropriate kernel.

In order to populate our cluster with galaxies, the following requirements were specified:

- (1) The total mass-to-light ratio of the cluster was chosen to be  $300h \text{ M}_\odot/\text{L}_\odot$ .
- (2) Galaxy luminosities  $L$  were drawn from a Schechter

function  $\Phi(L) \propto (L/L_\star)^\alpha e^{-(L/L_\star)}$  with  $L_\star = 10^{10}h^{-2} \text{ L}_\odot$ ,  $\alpha = -1$ , and a lower cutoff at  $0.1L_\star$ .

(3) Galaxy positions were randomly drawn from those of the N-body particles, so that ‘mass follows light’ in our model cluster.

This procedure resulted in a rich cluster of approximately 360 galaxies, about 45 of which are brighter than  $L_\star$ . The exact numbers vary for different random realizations.

For the mass distribution of the cluster galaxies, a simple truncated isothermal sphere model (Brainerd et al. 1996) was used. The surface mass density  $\kappa$  as a function of the projected radial distance  $\xi$  from the galaxy centre is given by

$$\kappa(\xi) = \frac{4\pi\sigma^2}{c^2} \frac{D_d D_{\text{ds}}}{D_s} \frac{1}{2\xi} \left( 1 - \frac{\xi}{\sqrt{s^2 + \xi^2}} \right), \quad (2)$$

and the cumulative mass can be calculated according to

$$M(<\xi) = \frac{\pi\sigma^2}{G} \left( \xi + s - \sqrt{s^2 + \xi^2} \right). \quad (3)$$

The two parameters, velocity dispersion  $\sigma$  and cutoff radius  $s$ , were chosen as functions of the galaxy luminosity according to the following scaling relations:

$$\sigma = \sigma_\star \left( \frac{L}{L_\star} \right)^{1/\eta} \quad \text{and} \quad s = s_\star \left( \frac{L}{L_\star} \right)^\nu. \quad (4)$$

For the first of these relations, which is motivated by the observed Tully-Fisher and Faber-Jackson relations, a value of  $\eta = 4$  was used for the scaling index. For simplicity, no distinction between spiral and elliptical cluster galaxies was made, and the velocity dispersion  $\sigma_\star$  of an  $L_\star$ -galaxy was fixed at an intermediate value of  $200 \text{ km/s}$ , which is closer to the value for early-type galaxies in order to take into account their dominance within galaxy clusters. The scaling relation for the cutoff radius is more conjectural, and choosing  $\nu = 0.5$  yields a mass-to-light ratio for the galaxies which is independent of luminosity. Another plausible parametrization would be to assume that the cutoff occurs at a fixed density of the dark matter halo, which would give  $s \propto \sigma$ . In order to test the performance of our analysis methods, which will be described in the next sections, we specified two models with different cutoff radii for the galaxy mass distribution. Choosing a low value of  $s_\star = 3.4h^{-1} \text{ kpc}$  gives a total  $L_\star$ -galaxy mass of  $M_\star = 10^{11}h^{-1} \text{ M}_\odot$ , corresponding to a total mass-to-light ratio of  $10h$  (in solar units) for the galaxies, whereas an extended halo of  $s_\star = 34h^{-1} \text{ kpc}$  results in  $M_\star = 10^{12}h^{-1} \text{ M}_\odot$  and a galaxy mass-to-light ratio of  $100h$ . For each of the two cases, the galaxy mass distributions were added to the global mass distribution from the numerical cluster simulation, which had been scaled such that the total mass of the system remains constant. Fig. 1 displays contour plots of the resulting surface mass density according to the two different galaxy models and illustrates their differences regarding the structure of the dark matter distribution.

Similarly, the shear corresponding to the total mass distribution can be obtained by adding the shear contribution from the individual galaxies to the (scaled) shear map calculated from the original surface mass distribution of the cluster. For the galaxy mass model of equation (2), the modulus of the shear is given by

**Figure 1.** The mass distribution for the simulated cluster of galaxies. The **top** panels show contours of the surface mass density corresponding to the two different models for the galaxy mass distribution. The **left** plot is for a cutoff radius of  $s_* = 3.4h^{-1}$  kpc, and the **right** one for  $s_* = 34h^{-1}$  kpc. Respectively, the **bottom** panels show the pattern of the average ellipticities of background galaxy images, overlaid with the reconstructed cluster mass distribution. The largest marks in these plots, indicating the strongest distortion effects, represent an average ellipticity of  $|\bar{\epsilon}| \approx 0.4$ . For clarity, the ellipticity patterns are displayed on a  $20 \times 20$  grid, whereas the reconstructions were calculated from a  $30 \times 30$  grid. Note that the same realization of background galaxies with the same intrinsic ellipticities was used for both cases, and therefore the reconstructed mass maps contain similar noise properties. The field of view is  $10'05$  and the contours are  $\kappa_\infty = 0.05, 0.1, 0.2, 0.3, 0.4, 0.5, 0.6, \dots, 1.2$ .

$$|\gamma|(\xi) = \frac{4\pi\sigma^2}{c^2} \frac{D_d D_{ds}}{D_s} \frac{1}{2\xi} \left( 1 + \frac{2s}{\xi} - \frac{2s^2 + \xi^2}{\xi\sqrt{s^2 + \xi^2}} \right), \quad (5)$$

and its phase can be determined from the position angle with respect to the galaxy centre.

## 2.2 Distortion Effects and Background Galaxies

For describing the ellipticities of galaxy images we use the complex parameter  $\epsilon$ , which is defined in terms of the second moments of the image brightness distribution (see, e.g., Seitz & Schneider 1997). In the special case of elliptical isophotes with axis ratio  $r \leq 1$ , its modulus is given by

$|\epsilon| = (1 - r)/(1 + r)$ . A graphical visualization of the ellipticity parameter space can be found in Fig. 5. The distortion effects exerted by the lens on the images of background galaxies do not depend on the parameters  $\kappa$  and  $\gamma$  individually, but only on the combined quantity ‘reduced shear’  $g = \gamma/(1 - \kappa)$ . The transformation of an intrinsic galaxy ellipticity  $\epsilon_s$  to the observable image ellipticity  $\epsilon$  is given by

$$\epsilon(\epsilon_s | g) = \begin{cases} \frac{\epsilon_s + g}{1 + g^* \epsilon_s} & \text{for } |g| \leq 1 \\ \frac{1 + g \epsilon_s^*}{\epsilon_s^* + g^*} & \text{for } |g| > 1, \end{cases} \quad (6)$$

with a case distinction between the even-parity ( $|g| < 1$ ) and the odd-parity ( $|g| > 1$ ) regions.

**Figure 2.** The modulus  $|g|$  of the reduced shear for the simulated cluster of galaxies (with  $s_\star = 34h^{-1}$  kpc). This quantity is a measure for the strength of the distortion effects (modulo the restrictions mentioned in the text). In order to emphasize the perturbations induced by the individual galaxies by increasing the contrast, a saturation value of  $|g| = 0.3$  was used for the grey scales. The plot was calculated for a source redshift of  $z = 1$ .

Fig. 2 shows a map of the modulus of the reduced shear for the simulated galaxy cluster described above. In the even-parity region this quantity is a measure for the strength of the distortion effects. The global mass distribution is non-critical, which means that  $|g| < 1$  everywhere, except very close to the centre of the individual cluster galaxies. In general, the image distortions tend to be aligned tangentially towards the centre of mass concentrations. The figure illustrates the perturbing effects of the individual cluster galaxies. At their positions in a radial direction towards and away from the cluster centre, the strength of the distortion is locally increased because the effects of the global cluster mass distribution and the individual galaxies then act in the same direction. But in the direction tangential to the cluster centre, the orientation of the galaxy contribution to the shear is perpendicular to the shear direction of the cluster, and

therefore these effects partly cancel, leading to a reduction in the strength of the distortion effects.

However, Nature does not provide us with a continuous map of the lensing properties, but only with very noisy estimates of the reduced shear at the discrete positions of background galaxy images. For these simulations, a population of background galaxies was generated with a number density of  $40/\text{arcmin}^2$ . Their intrinsic ellipticities were drawn from a probability distribution of the form

$$p_{\epsilon_s}(\epsilon_s) = \frac{1}{\pi \sigma_{\epsilon_s}^2 (1 - e^{-1/\sigma_{\epsilon_s}^2})} e^{-(|\epsilon_s|/\sigma_{\epsilon_s})^2} \quad (7)$$

with dispersion  $\sigma_{\epsilon_s} = 0.2$ , and their positions were randomly distributed within the field of view.

Up to now we did not specify the redshifts of the source galaxies, and the discussion above assumed them to be located in a single redshift plane. The strength of the lensing

effect depends on the source redshift via the angular diameter distances appearing in the definition of the critical surface mass density in equation (1). We adopt the approach of Seitz & Schneider (1997) and relate the lensing parameters to their respective values corresponding to (hypothetical) sources located at infinite redshift. The surface mass density and the shear as a function of source redshift  $z$  can then be expressed as  $\kappa(z) = w(z)\kappa_\infty$  and  $\gamma(z) = w(z)\gamma_\infty$ , and for an Einstein-de Sitter universe the ‘relative lensing strength’ can be calculated as

$$w(z) = \begin{cases} 0 & \text{for } z \leq z_d \\ \frac{\sqrt{1+z} - \sqrt{1+z_d}}{\sqrt{1+z} - 1} & \text{for } z > z_d \end{cases} . \quad (8)$$

The reduced shear as a function of source redshift is given by

$$g(z | \kappa_\infty, \gamma_\infty) = \frac{w(z)\gamma_\infty}{1 - w(z)\kappa_\infty} , \quad (9)$$

and therefore the statistical properties of the lensing effect depend on the surface mass density  $\kappa_\infty$  and the shear  $\gamma_\infty$  explicitly, although the degeneracy mentioned earlier is only weakly broken as long as the lens is non-critical for all redshifts. For each of the source galaxies a redshift was drawn from the probability distribution (Brainerd et al. 1996)

$$p_z(z | z_0, \beta) = \frac{\beta z^2}{\Gamma(\frac{3}{\beta}) z_0^3} e^{-(z/z_0)^\beta} \quad (10)$$

with  $z_0 = 1/3$  and  $\beta = 1$  which results in an average redshift of  $\langle z \rangle = 1$ . The observable image ellipticities were then calculated by applying equations (8), (9), and (6). Some of our source galaxies are in fact unlensed foreground objects, but for simplicity the entire population generated in this way is referred to as ‘background galaxies’. The lensing effects of background galaxies on the images of more distant galaxies within that population are neglected in this study.

Whenever we use the quantities  $\kappa$ ,  $\gamma$ , or  $g$  without redshift-argument or  $\infty$ -subscript in the rest of the paper, this should be regarded as referring to a single redshift plane.

### 2.3 Cluster Mass Reconstruction

Assuming that we can unambiguously distinguish the cluster galaxies from the population of background galaxies, we calculated the average image ellipticity  $\bar{\epsilon}$  for the latter on a  $30 \times 30$  grid using a Gaussian smoothing procedure with variable smoothing length in order to account for the varying strength of the distortion effects. For simplicity, this smoothing length was adjusted linearly from  $0.2'$  at the cluster centre to  $1.0'$  at the boundary of the field of view, although in principle objective strategies could be developed for its optimal choice. Fig. 1 displays the gridded distortion pattern determined in this way, as well as the reconstruction of the cluster surface mass density calculated from it by applying the non-linear finite-field inversion method described in Seitz & Schneider (1996), and taking into account the redshift distribution of the sources as explained in Seitz & Schneider (1997). Here we assumed the true redshift distribution to be known, and we will comment on the consequences of giving up this assumption in Section 4.6.

The figure reveals that there are only minor differences in the reconstructed cluster mass distribution for the two

different galaxy mass models. The information contained in the background galaxy images about the structure of the mass distribution on galaxy scales is very efficiently erased by the averaging procedure described above. In reconstructions performed with a refined grid and reduced smoothing length for the galaxy input model with large cutoff radius, it is sometimes possible to identify reconstructed mass clumps with groups of massive galaxies. However, a quantitative analysis of the significance of sub-clumps in mass maps is extremely difficult, and therefore this does not seem to be a practical method to constrain the mass distribution of cluster galaxies.

Analysing the weak distortions of background galaxies only allows the mass distribution of the lens to be determined up to a global invariance transformation of the form

$$\kappa(\vec{\xi}) \rightarrow (1 - \kappa_s) \kappa(\vec{\xi}) + \kappa_s , \quad (11)$$

which corresponds to adding a sheet of constant surface mass density  $\kappa_s$  after appropriately rescaling the reconstructed solution (Falco, Gorenstein & Shapiro 1985, Schneider & Seitz 1995). For practical purposes this degeneracy remains even if the sources are distributed in redshift. In this case transformations similar to equation (11) apply (Seitz & Schneider 1997). In our simulations we artificially adjusted the reconstructed surface mass density such that the total mass of the cluster is correctly reproduced. In practice, the ‘mass sheet degeneracy’ can be broken by postulating that the surface mass density of a reasonable galaxy cluster should have dropped to insignificant values at the boundaries of a large field of view, or by exploiting magnification effects, either through the lensing effects on the number counts of background galaxies (Broadhurst, Taylor & Peacock 1995) or the size-magnitude relation (Bartelmann & Narayan 1995), which are not invariant under the transformation (11).

Another technical difficulty is the following: In addition to the reconstructed surface mass density, the likelihood method to be described in Section 4 also requires a map of the shear which corresponds to this mass distribution. However, calculating the shear from the surface mass density *a posteriori* involves an integration extending beyond the limited data region. Again, there will be no practical problems, if the surface mass density attains negligible values at the boundary of the field of view, provided that there are no huge mass clumps lurking just outside of it.

## 3 $\zeta$ -STATISTIC

### 3.1 Theory

Kaiser (1995) showed that the difference of the average surface mass densities within a circular aperture  $\bar{\kappa}(x_1)$  and an annulus around that aperture  $\bar{\kappa}(x_1, x_2)$  can be calculated from the shear within the annulus:

$$\zeta(x_1, x_2) := \bar{\kappa}(x_1) - \bar{\kappa}(x_1, x_2) = \frac{2x_2^2}{x_2^2 - x_1^2} \int_{x_1}^{x_2} \frac{dx}{x} \langle \gamma_t \rangle(x) . \quad (12)$$

The variable  $x$  represents a radial coordinate measured from the centre of the aperture, and  $x_1$  and  $x_2$  denote the inner and the outer radius of the annulus, respectively.  $\gamma_t$  is the tangential component of the shear and  $\langle \gamma_t \rangle(x)$  is its circularly averaged value as a function of the radial distance. This

equation was first applied by Fahlman et al. (1994) in order to determine a rigorous lower limit on the mass of the galaxy cluster MS1224, without the need to worry about non-linear lensing properties or the confusion of background and cluster galaxies in the cluster centre. In this section we investigate the possibilities offered by this method for obtaining information on the mass distribution of cluster galaxies. This can be achieved by analysing the distortion of background galaxy images in annuli centred on individual cluster galaxies and adding the effects of a large number of them in order to get a significant signal. A nice feature of this application of relation (12) is that the reference to the surface mass density in the annulus automatically takes into account an underlying cluster mass distribution and directly measures the galaxy masses, provided the surface mass density of the cluster can be reasonably approximated locally as a linear function. It is easy to see that a linear trend in the cluster mass profile does not affect  $\bar{\kappa}(x_1, x_2)$  and so only higher order variations of the cluster mass distribution on scales comparable to the size of the annulus could bias the mass measurement.

The right-hand-side of equation (12) can be written as a two-dimensional integral and, therefore, be approximated by a sum over the discrete data points which are provided by the images of background galaxies:

$$\zeta(x_1, x_2) \approx x_2^2 \frac{1}{N} \sum_{i=1}^N \frac{\gamma_{ti}}{x_i^2} \approx x_2^2 \frac{1}{N} \sum_{i=1}^N \frac{\epsilon_{ti}(1-\kappa_i)}{x_i^2}. \quad (13)$$

With our definition for the ellipticity parameter  $\epsilon$ , the expectation value for observed image ellipticities is equal to the reduced shear:  $\langle \epsilon \rangle_{\epsilon_s} = g$  (Schramm & Kayser 1995, Seitz & Schneider 1997). Therefore, each observed image ellipticity  $\epsilon_i$  is an unbiased – though very noisy – estimate for the reduced shear  $g_i = \gamma_i/(1-\kappa_i)$  at the image position, and  $\gamma_{ti}$  can be replaced by  $\epsilon_{ti}(1-\kappa_i)$  in the above equation. (Here we restricted the treatment to the even-parity region; in the odd-parity case  $\langle \epsilon \rangle_{\epsilon_s} = 1/g^*$ .) In the limit  $\kappa \ll 1$  the shear can be directly estimated from the image ellipticities ( $\langle \epsilon \rangle_{\epsilon_s} \approx \gamma$ ) and no further information about the cluster mass distribution is required for applying the  $\zeta$ -statistic. When leaving the linear regime, however, the corrective factor  $(1-\kappa)$  becomes important. In this case, the surface mass density  $\kappa_i$  at the image positions can be taken from a reconstruction of the cluster mass distribution.\* [Performing a mass sheet transformation of the reconstructed mass distribution according to equation (11) modifies  $\zeta$  and all galaxy mass estimates derived from it by a factor  $(1-\kappa_s)$ . This can easily be seen by replacing  $\kappa_i$  with  $(1-\kappa_s)\kappa_i + \kappa_s$  in equation (13).]

The calculation of  $\zeta$  according to equation (13) can be regarded as a kind of noisy Monte-Carlo integration. Both of the two approximate-equality signs only hold for a rather large number  $N$  of background images and become equalities

\* The ‘radial averaging method’ employed by Natarajan and Kneib (1997) is similar to the one described here, but it does not include the extension into the non-linear lensing regime provided by the  $(1-\kappa)$ -factor. Whereas this omission does not preclude the significant detection of a lensing signal by cluster galaxies, it renders a quantitative interpretation more indirect.

for  $N \rightarrow \infty$ . They express two different kinds of uncertainties; the first one those which are arising from sparse sampling of the integration area, and the second one those from the noisy data points. The errors in  $\zeta$  due to the latter may be expressed in terms of the intrinsic ellipticity dispersion  $\sigma_{\epsilon_s}$  as

$$\sigma[\zeta(x_1, x_2)] \approx x_2^2 \frac{\sigma_{\epsilon_s}}{\sqrt{2}} \frac{1}{N} \left( \sum_{i=1}^N \frac{(1-\kappa_i)^2}{x_i^4} \right)^{\frac{1}{2}}, \quad (14)$$

which is not quite exact, because lensing changes the dispersion of the probability distribution for the observed image ellipticities (see Section 4.2). Due to the rather inhomogeneous shear pattern which is induced by the cluster galaxies (see Fig. 2), the errors from the sparse sampling of the integration area may also be substantial in our application of the  $\zeta$ -statistic, and as  $\kappa_i$  approaches unity those introduced by an inaccurate reconstruction of the cluster mass distribution will become important as well.

The discussion so far assumed a single redshift plane for the background sources. In the case of a redshift distribution, the equations are still valid for  $\kappa_i \ll 1$ , if the surface mass density and the shear are interpreted as quantities referring to the redshift-averaged critical surface mass density, which means  $\kappa = \langle w \rangle_z \kappa_\infty$  and  $\gamma = \langle w \rangle_z \gamma_\infty$ . But in the non-linear regime, the treatment should be generalized, because then the expectation value for observed image ellipticities also depends on higher moments of the redshift distribution. Seitz & Schneider (1997) derived the approximation

$$\langle \epsilon \rangle_{\epsilon_s, z} \approx \frac{\langle w \rangle_z \gamma_\infty}{1 - \frac{\langle w^2 \rangle_z}{\langle w \rangle_z} \kappa_\infty}, \quad (15)$$

which is quite accurate for  $\kappa_\infty \lesssim 0.8$  and generic redshift distributions. In analogy to the calculations above, this offers an estimate for the tangential shear in terms of the observed image ellipticities (and the reconstructed cluster mass distribution), and expressions equivalent to equations (13) and (14) can be computed. In the application to the simulations we employed this slightly generalized formalism.

### 3.2 Application to Simulations

The radial mass profile of the cluster galaxies can be probed by calculating the  $\zeta$ -statistic as a function of the inner radius of the annulus. The minimal inner radius for applying this method is limited by the ability to measure reliable ellipticities for background galaxy images in the vicinity of the typically much brighter cluster galaxies. Another, theoretical complication for images located very close to cluster galaxies is that those also contribute to the surface mass density at the image positions, and this should in principle be included in the corrective factor  $(1-\kappa_i)$  as well, which requires specifying a model for the galaxy mass distribution. However, this problem can be neglected in view of the observational limitations mentioned above, because at useful radial distances the surface mass density of the cluster galaxies should already have dropped to insignificant values.

The outer radius of the annulus must not be so large that the reference-term  $\bar{\kappa}(x_1, x_2)$  picks up variations of the cluster mass distribution. In practice, a more serious limitation for its extent is the presence of neighbouring cluster galaxies, which must not be located within the annulus

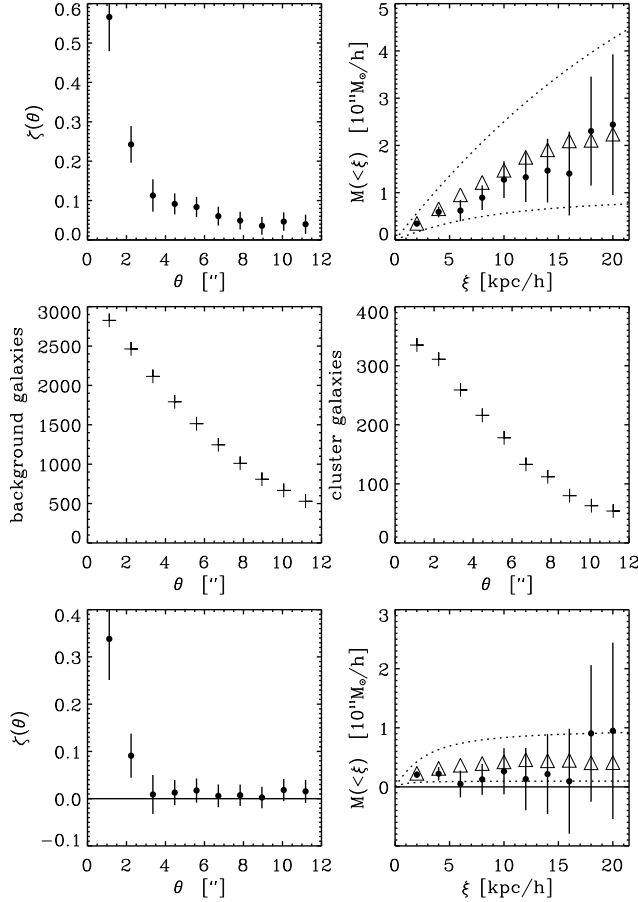


**Figure 3.** Application of the  $\zeta$ -statistic to the simulations. The plots show  $\zeta$  and the aperture mass measurements derived from it as a function of the (inner) aperture radius. The **top** panels are for the input galaxy mass model with a large cutoff radius of  $s_* = 34h^{-1}$  kpc and the **bottom** panels for the model without extended dark matter halo ( $s_* = 3.4h^{-1}$  kpc). Regardless of their luminosity, cluster galaxies were included in the analysis according to the criterion described in the text. The triangles denote the average mass of the included cluster galaxies and therefore represent the quantity which is supposed to be measured by the lensing estimates. For orientation, the dotted lines show the mass profile of an  $0.1L_*$ - and an  $L_*$ -galaxy according to the respective input model. The **middle** panels display the number of background and cluster galaxies used in the analysis.

in order to keep  $\bar{\kappa}(x_1, x_2)$  as small as possible. As long as these constraints are satisfied,  $\bar{\kappa}(x_1, x_2)$  and therefore also  $\zeta(x_1, x_2)$  are nearly independent of the outer radius  $x_2$ . This means that the outer radius can be chosen individually for each cluster galaxy and still the  $\zeta$ -estimates from each of those can be combined afterwards to achieve significant results. In order to use the available information effectively, we therefore adopted the following strategy for calculating the mass estimates for a given value of the inner radius. Cluster galaxies were included in the analysis, if inner-radius circles centred on them did not intersect the inner-radius circle drawn around any other cluster galaxy. (This leads to a bias of the positions of the included cluster galaxies away from the cluster centre.) For each of the cluster galaxies used, the outer radius was then specified as the maximal radius possible without intersecting the *inner*-radius circle around

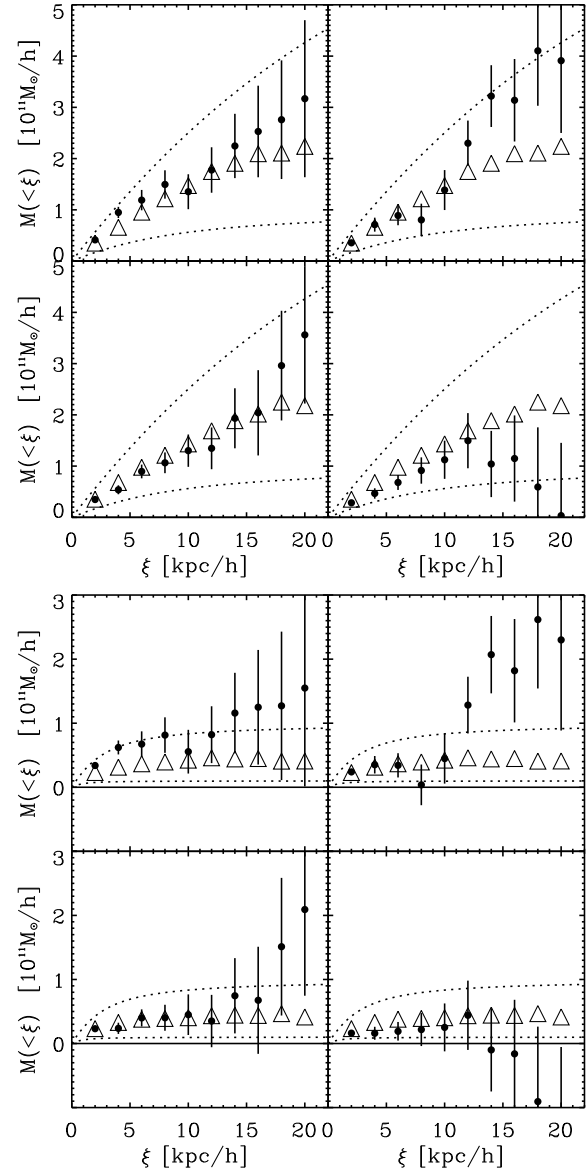


**Figure 4.** Mass estimates from the  $\zeta$ -statistic for different realizations of cluster and background galaxies. The four diagrams at the **top** are for the input model with large cutoff radius and the **bottom** ones for the small cutoff radius. (As mentioned in the text, the innermost data point in these plots can be systematically affected by a non-negligible cluster galaxy contribution to the surface mass density at the image positions, and in practice, the determination of this data point will be hampered by observational problems.)

any other cluster galaxy. With this prescription, some background galaxy images located between cluster galaxies have to be included in the analysis twice or several times, with reference to different cluster galaxies. Note that the method implicitly takes into account the shear effects of more than one cluster galaxy on individual background images.

The radial coordinate  $x$  used so far can either be regarded as an angular separation  $\theta$  on the sky or as the projected physical separation  $\xi = D_d \theta$  in the lens plane. For a given inner radius, the  $\zeta$ -value can be trivially converted into an estimate of the projected mass within that aperture:

$$M(<\xi) = \pi \xi^2 \zeta(\xi) \Sigma_{\text{crit}} . \quad (16)$$

Fig. 3 displays the results of applying the method to the simulations described in Section 2. The plots of this figure reveal that the signal-to-noise ratio of the aperture mass measurement rapidly deteriorates for increasing aperture radius, because the number of background and cluster galaxies which can be used for the analysis then considerably decreases. The error bars drawn in the figure, which are of course correlated for different data points, were calculated according to equation (14) and only include the uncertainties due to the intrinsic ellipticity distribution of the sources. More comprehensive error estimates could be computed from the simulations. In order to give an indication of the true errors for the mass determination, Fig. 4 depicts the results for different realizations of cluster and background galaxies. To be specific, we selected two realizations from a sample of five random sets of background galaxies and combined them with two different random realizations of cluster galaxies. For the galaxy mass model with a large cutoff radius, significant mass detections are feasible up to radial distances of  $\approx 15h^{-1}$  kpc. For the model with a small cutoff radius, however, it is hardly possible to achieve significant results at all. Nevertheless, the data still allow us to set limits on the presence of an extended dark matter halo in this case.

In the application of the  $\zeta$ -statistic to the simulations we mainly concentrated on exploring the capabilities of the method for reliably retrieving the input values, and in view of the more powerful techniques to be described in the next section, we do not further discuss the optimal strategies for quantifying or interpreting the results provided by it.

The  $\zeta$ -statistic allows us to determine a direct galaxy mass estimate without any model assumptions, and it can be conveniently applied in the outskirts of a cluster where the separations between the cluster galaxies are large. However, due to geometrical constraints the method cannot make optimal use of all the information available; in particular, it is not well suited to test the radial extent of the galaxy mass distribution. Towards the cluster centre, the crowding of cluster galaxies seriously compromises the applicability of the method. In addition to that, the generalization to the non-linear regime removes much of the  $\zeta$ -statistic's original simplicity, and an accurate description of the global cluster mass distribution becomes important.

## 4 MAXIMUM LIKELIHOOD METHOD

### 4.1 Model Specification

The maximum likelihood method described here follows in part the prescription of Schneider & Rix (1997) for weak lensing by field galaxies. The principle philosophy of likelihood techniques is to specify a model, calculate the probability distribution of observable quantities according to the model, and maximize the joint probability density for the actually observed values by varying the model parameters. In our case, the observable image distortions are a consequence of the interplay between the effects of a global cluster potential and the perturbations due to individual galaxies. In addition to specifying a parametrized mass model for the galaxies, it is therefore important to have an accurate de-

scription of the cluster mass distribution which is provided by the reconstruction presented in Section 2.3.

As a model for the galaxy mass distribution we again use the truncated isothermal sphere (2). Of course, this model is appropriate for the synthetic data used here, whereas one could argue that realistic galaxy haloes in clusters might rather be flattened or completely irregular. However, this analysis is aimed at determining the average properties of an ensemble of galaxies which might still be reasonably well described by a simple model with a characteristic scale and normalization as parameters. In order to add the information from galaxies with different luminosities, the scaling relations (4) were applied. Adding the mass models for each of the cluster galaxies to the cluster reconstruction then yields a model for the total mass distribution of the system as a function of the model parameters, which are the velocity dispersion  $\sigma_*$  and the cutoff radius  $s_*$  of an  $L_*$ -galaxy, and the scaling indices  $\eta$  and  $\nu$ . Analogously, the shear contribution due to the galaxies, which is given by equation (5), can be added to the global shear from the reconstruction (see Section 2.3) in order to obtain the total shear corresponding to the total mass model.

A complication which has to be taken into account when performing this procedure is the following: If the individual galaxies do have extended haloes, the mass in galaxies constitutes a significant fraction of the total cluster mass. The cluster reconstruction is sensitive to the total mass, and therefore it already includes the (smoothed-out) mass contribution from the galaxies. This means that the additional mass added by the galaxy models has to be compensated in some way. This was done by simply scaling down the reconstruction appropriately or by subtracting surplus mass locally at the position of cluster galaxies. The merits and limitations of these (*ad hoc*) procedures will become evident in Section 4.4.

The total mass model constructed in this way determines the values for the lensing quantities  $\kappa_\infty$  and  $\gamma_\infty$  at the position of each background galaxy image as a function of the galaxy model parameters. Given the surface mass density and the shear, the next section deals with the problem of calculating the probability density distributions for image ellipticities.

### 4.2 Probability Density Distributions

In the case of a single redshift plane for the background galaxies, the probability density for observing an image ellipticity  $\epsilon$  is given by

$$p_\epsilon(\epsilon | g) = p_{\epsilon_s}(\epsilon_s(\epsilon | g)) \left| \frac{d^2\epsilon_s}{d^2\epsilon} \right| (\epsilon | g) , \quad (17)$$

and it is completely specified by the reduced shear at the image position.<sup>†</sup> The transformation  $\epsilon_s(\epsilon | g)$  of image to source ellipticities can be obtained by inverting equation (6), and the Jacobian determinant of this transformation can be computed according to

<sup>†</sup> Note that the Jacobian determinant in (17) has been left out in Natarajan & Kneib (1997).

$$\left| \frac{d^2 \epsilon_s}{d^2 \epsilon} \right| (\epsilon | g) = \begin{cases} \frac{(|g|^2 - 1)^2}{|\epsilon g^* - 1|^4} & \text{for } |g| \leq 1 \\ \frac{(|g|^2 - 1)^2}{|\epsilon - g|^4} & \text{for } |g| > 1. \end{cases} \quad (18)$$

[In the limit  $|g| \ll 1$ , the ellipticity transformation reads  $\epsilon \approx \epsilon_s + g$ , and the Jacobian determinant reduces to unity. The lensed probability density distribution is then approximately equal to the intrinsic one shifted in the shear direction:  $p_\epsilon(\epsilon | g) \approx p_{\epsilon_s}(\epsilon - g)$ .]

However, if the sources are distributed in redshift, the reduced shear has to be calculated from  $\kappa_\infty$  and  $\gamma_\infty$  as a function of redshift according to equation (9). In this case, the probability density for observing an ellipticity  $\epsilon$  can be obtained by integrating equation (17) over redshift

$$p_\epsilon(\epsilon | \kappa_\infty, \gamma_\infty) = \int_0^\infty dz p_z(z) p_{\epsilon_s}(\epsilon_s(\epsilon | \kappa_\infty, \gamma_\infty, z)) \left| \frac{d^2 \epsilon_s}{d^2 \epsilon} \right| (\epsilon | \kappa_\infty, \gamma_\infty, z) \quad (19)$$

and it explicitly depends both on the surface mass density and on the shear. In order to calculate this probability density in practice, it is necessary to know the intrinsic ellipticity distribution  $p_{\epsilon_s}(\epsilon_s)$  of the sources, which we assume to be available from observations in ‘empty fields’. (A possible dependence of the intrinsic distribution on the redshift, the magnitude, or other galaxy characteristics could easily be taken into account in the above equation.) A more serious problem is to specify an estimate for the redshift distribution of the sources. As was mentioned in Section 2.3 we use the true  $p_z(z)$  within our analysis, and discuss the consequences of an incorrect redshift distribution in Section 4.6.

Fig. 5 illustrates the modification of the ellipticity distribution induced by lensing. In the case of a fixed source redshift, the lensed distribution has the nice property that the expectation value of the image ellipticities recovers the reduced shear, which has already been used in Section 3. The dispersion of the ellipticity distribution is reduced compared to the intrinsic one, and although the distribution becomes skewed, its contour lines remain fairly circular. In fact, it can be shown that the dispersion of the distribution in ‘shear direction’ (along the  $\epsilon_1$ -axis in the plot) is equal to the dispersion perpendicular to this direction in the ellipticity coordinates (along the  $\epsilon_2$ -axis in the plot). In the presence of a redshift distribution, the probability density distribution for the image ellipticities becomes elongated along the ‘shear direction’, because the strength of the distortion effect depends on the redshift of the sources. The images of galaxies located just behind the lens are only slightly affected, and obviously foreground objects are not distorted at all.

For completeness, the figure also illustrates the ellipticity distribution for lens parameters which are critical for sufficiently high redshifts. In this case,  $p_{\epsilon_s}(\epsilon_s)$  formally includes a  $\delta$ -‘function’ contribution at ellipticity coordinates corresponding to arcs. For a ‘radially critical’ lens, images can either be distorted tangentially or radially, depending on the source redshift, and in principle a radial and a tangential arc could be superposed at the same position on the sky.

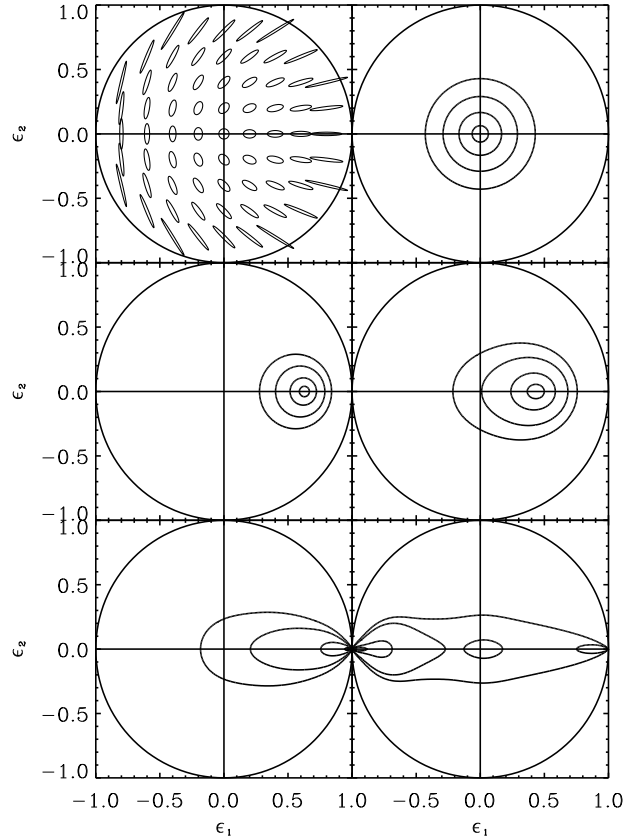


**Figure 5.** The probability density distribution for image ellipticities. The **top left** plot is a graphical visualization of the ellipticity parameter  $\epsilon = \epsilon_1 + i\epsilon_2$ . It displays the shape of the images of an intrinsically circular source. The **top right** plot shows the isotropic probability density distribution for the intrinsic shape of background galaxies [equation (7) with  $\sigma_{\epsilon_s} = 0.2$ ]. The contour lines in this and in the following plots enclose 99%, 90%, 50%, and 10%, respectively, of the probability. The other four diagrams display the probability density distribution for the image ellipticity of lensed background galaxies. The **middle left** plot is for  $g = 0.6$  and single redshift sources, and the **middle right** one for  $\gamma_\infty = 0.3$ ,  $\kappa_\infty = 0.5$  and a redshift distribution of the sources according to equation (10) with  $\beta = 1$  and  $\langle z \rangle = 1$ . The lens redshift is  $z_d = 0.16$ . Note that we chose real  $g$  and  $\gamma_\infty$  values for this illustration, which specifies the  $\epsilon_1$ -axis as the ‘shear direction’. The **bottom** plots show the ellipticity distributions for lens parameters which are ‘tangentially critical’ (**left**,  $\gamma_\infty = 0.4$ ,  $\kappa_\infty = 0.8$ ) and ‘radially critical’ (**right**,  $\gamma_\infty = 0.6$ ,  $\kappa_\infty = 2.0$ ) with the same redshift distribution as above. (In the bottom plots the 10%-contour line is not visible in this representation.)

### 4.3 Likelihood Function and Confidence Contours

The likelihood function  $\mathcal{L}$  can now be defined as the product of the probability densities of the actually measured ellipticities  $\epsilon_i$  of all the background galaxy images

$$\mathcal{L}(\sigma_\star, s_\star, \eta, \nu) := \prod_i p_\epsilon(\epsilon_i | \kappa_{\infty i}, \gamma_{\infty i}), \quad (20)$$

and it depends on the galaxy model parameters via the mass model specification discussed in Section 4.1. The logarithm of the likelihood function is denoted as  $l := \ln \mathcal{L}$ .

Fig. 6 demonstrates the application of the likelihood analysis to the simulated data for the input model with the

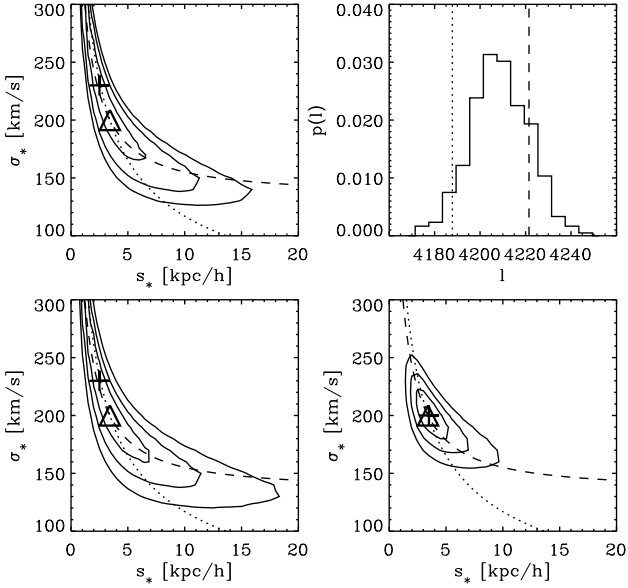


**Figure 6.** Application of the maximum likelihood method to the simulations with small cut-off radius. For this particular realization, the analysis includes 3969 background galaxy images and 367 cluster galaxies. The **top left** plot displays the logarithm of the likelihood as a function of the velocity dispersion  $\sigma_*$  and the cutoff radius  $s_*$ . The contours are  $\Delta l := l - \text{Max}(l) = -5, -3, -1$ . The triangle denotes the input values and the cross marks the maximum of the likelihood function. The dotted line connects models with equal total mass, and along the dashed line the mass within a projected radius of  $5.4h^{-1}$  kpc is constant. The histogram on the **top right** depicts the probability distribution for the value of  $l$  calculated from the correct mass distribution. The dashed vertical line indicates the value  $\text{Max}(l)$  at the maximum of the likelihood function for the particular realization, and the dotted vertical line represents the likelihood of the reconstruction without galaxies added. For the **bottom** diagrams the likelihood contours were transformed into confidence regions as explained in the text. The **left** plot is without prior information, and the **right** one includes *a priori* knowledge of  $\sigma_* = 200 \pm 15$  km/s. The confidence contours are 99.73%, 95.4%, and 68.3%.

small cutoff radius of  $s_* = 3.4h^{-1}$  kpc. Here we investigated the dependence of the likelihood function on the velocity dispersion  $\sigma_*$  and the cutoff radius  $s_*$ , keeping the scaling indices fixed at their input values. The analysis includes the background galaxy images from the entire field of view, except those which are located very close to cluster galaxies and which are therefore likely to be unobservable in practice. More specifically, an angular separation limit of  $\sqrt{L/L_*} 3''$  was employed, whereby  $L$  denotes the cluster galaxy luminosity. Hence, in this study there is no lensing information available on the mass distribution of cluster galaxies within a projected radius of  $D_d 3'' \approx 5.4h^{-1}$  kpc. In fact, the likelihood contours closely follow the line of models with equal mass within this radius, and therefore this is the quantity which can be determined best with this lensing method, while the velocity dispersion and the cutoff radius cannot be well constrained individually.

In order to verify the absolute likelihood level of the reconstructed mass model, the figure also shows the probability distribution for  $l$  calculated with the correct input mass distribution from many different realizations of intrin-

sic background galaxy ellipticities. In accordance with the central limit theorem, this histogram is consistent with a Gaussian distribution. The maximum of the likelihood function lies well within this distribution, and therefore the total mass model, consisting of the reconstructed cluster mass distribution plus the galaxy mass model, is statistically consistent with the observed image ellipticities.

The likelihood contours can be transformed into confidence regions for the model parameters. The procedure we adopted to achieve this will be explained at the end of this section. Using only the information provided by the lensing analysis allows to set an upper limit on the cutoff radius of about  $18h^{-1}$  kpc in the example case depicted in Fig. 6. However, large values for the cutoff radius  $s_*$  are only compatible with unrealistically low values for the velocity dispersion  $\sigma_*$ . As a consequence, it is possible to achieve much tighter limits on  $s_*$  by making use of *a priori* knowledge on  $\sigma_*$ . If we believe that the measured velocity dispersions of elliptical galaxies or the rotational velocities of spirals (divided by a factor of  $\sqrt{2}$ ) represent the same quantity as the parameter  $\sigma$  of the dark matter halo model, we can include this knowledge into the analysis. The likelihood function can be regarded as the joint probability distribution  $p(\epsilon_1, \dots, \epsilon_N | \sigma_*, s_*)$  of observing the image ellipticities for a given set of model parameters. According to Bayes' Theorem, the probability distribution for the parameters is then given by

$$p(\sigma_*, s_*) \propto p_{\text{prior}}(\sigma_*, s_*) p(\epsilon_1, \dots, \epsilon_N | \sigma_*, s_*) , \quad (21)$$

and the constant of proportionality is fixed by requiring the proper normalization. Confidence regions for the parameters can be found by determining the contour lines which enclose a given fraction of the total probability. The figure displays the result after taking into account the prior information of  $\sigma_* = 200 \pm 15$  km/s which makes it possible to derive very interesting limits on  $s_*$ . By specifying a constant prior, the Bayesian reasoning also allows us to transform the likelihood contours into confidence regions without *a priori* information. The corresponding plot in the figure was already mentioned above. (Strictly speaking, the prior used in this case is constant only over the region covered by the plot, but zero for parameter values not represented by it.)

#### 4.4 Velocity Dispersion and Cutoff Radius

Fig. 7 shows confidence regions (without including prior information) for the velocity dispersion and the cutoff radius, computed for several realizations of cluster and background galaxies. Here we divided the data into two independent subsets according to the position of the background galaxy images. In one case we included all images ( $\approx 3740$ ) located outside of a square with side length  $2.5'$  centred on the peak of the cluster mass distribution, and the second case includes all images ( $\approx 240$ ) within this central region. The number of cluster galaxies which are located in these areas are  $\approx 270$  and  $\approx 90$ , respectively. Again, the exact numbers are varying for different random realizations.

We start the discussion with the results for the galaxy input model with small cutoff radius. In this case, the galaxies contribute only about three per cent to the total mass of the galaxy cluster and the mass compensation procedure mentioned in Section 4.1 is not very important. The figure

shows that the far fewer images in the centre provide almost the same amount of information as the numerous images in the outskirts of the cluster. The reasons for this are the higher cluster galaxy density in the centre and the significant enhancement of the distortion effects of individual cluster galaxies due to the underlying cluster mass distribution. However, the confidence regions for this central subset of the data depend somewhat on the details of the reconstruction procedure. In particular, the smoothing length must not be too large and the reconstruction grid must not be too coarse in order to prevent the cluster's central peak from being smeared out in the mass reconstruction.

For the model with an extended dark matter halo with cutoff radius  $s_* = 34h^{-1}$  kpc, about one third of the total mass of the system is contained in the galaxies, and therefore the prescription for the mass compensation becomes extremely important. In regions of low surface mass density, it turned out that the most effective procedure is to subtract mass locally at the position of the cluster galaxies in the form of Gaussian distributions with widths corresponding to the (local) smoothing scale used for calculating the gridded image ellipticities. This is applicable as long as the subtracted mass fraction is not exceedingly large. For the subset of the data regarding the outskirts of the cluster, the results presented in Fig. 7 indicate that the velocity dispersion  $\sigma_*$  can be retrieved reasonably well in this case, whereas it is more difficult to constrain the radial extent of the galaxy mass distribution. However, the rather arbitrary mass subtraction procedure is certainly not optimal, and the additional uncertainties arising from it are not included in the confidence regions, because the maximum likelihood method described here assumes that the description of the 'global cluster mass distribution' constructed in that way is correct. Nevertheless, a robust lower limit of typically about  $10h^{-1}$  kpc can be set for the cutoff radius, and so this model can be distinguished with high significance from the low- $s_*$  model discussed above. The upper limits, on the other hand, are more sensitive to the details of the mass compensation procedure. (Formally, a strict upper limit can be derived from the fact that the total mass is fixed by the cluster reconstruction. In our simulations, for example, a galaxy model with  $\sigma_* = 200$  km/s and  $s_* \approx 100h^{-1}$  kpc accounts for all the mass in the system.)

For the input model with massive galaxies, it is worth to note that there is a very large difference ( $\Delta l \approx 150$ ) in the likelihood values between the best-fit model with galaxies and the pure reconstruction map without any cluster galaxies included, and in contrast to the model without extended galaxy halo (see the plot in Fig. 6) the pure reconstruction is not consistent with the observed image ellipticities in an absolute likelihood sense.

The problems of the method become apparent in the diagrams of Fig. 7 depicting the results for the central cluster region. Here, the input values for the galaxy model parameters cannot be reliably recovered, and in addition, the confidence regions change considerably when the strategy for the mass compensation is modified. (For the plots shown in the figure, the cluster mass reconstruction was scaled down by the mass fraction put into galaxies in order to conserve the total mass.) In the outer regions of the cluster, the problem is less severe, because the requirements for the accuracy of the cluster mass reconstruction are less stringent when the

surface mass density is low, and so the method works there reasonably well even when the galaxies are massive. In the highly non-linear lensing regime of the cluster centre, however, an accurate description of the cluster mass distribution is essential to obtain reliable results. From our investigations we conclude that the cluster reconstruction and the maximum likelihood analysis for inferring the properties of the cluster galaxies cannot be performed independently, taking the results of the former as an input for the latter. Instead, both procedures have to be performed at the same time. To this end we employed a maximum likelihood reconstruction of the cluster mass distribution in the fashion of Bartelmann et al. (1996). In such a method the presence of cluster galaxies can be taken into account explicitly during the reconstruction process. For each set of parameters of the galaxy mass model, one can then determine the best representation of the underlying cluster mass distribution. Therefore, this approach is also more satisfactory in a full maximum likelihood sense. A regularization of the cluster mass distribution (for example by an entropy-like term) prevents it from exhibiting structures on galaxy scales and thus allows the separation between galaxy mass components and the underlying cluster mass distribution. That method and its application to our simulations will eventually be presented in a separate publication.

Distinguishing between the dark matter associated with galaxy haloes and dark matter belonging to a 'global cluster mass distribution' poses not only a technical problem, but also a conceptual one. Especially towards the centre of galaxy clusters where the physical distances between the galaxies become very small, making this distinction becomes somewhat artificial, and clearly the giant cD-galaxies residing in the centre of many clusters cannot be treated with the same formalism as ordinary cluster galaxies.

Although the general formulation of our method in principle allows the treatment of critical clusters as well, we restricted the application in this paper to the non-critical case, because otherwise the problems for the cluster centre alluded to above would be substantially more serious. For the critical regions it is indispensable to model the mass distribution of a global component and those of individual cluster galaxies simultaneously.<sup>‡</sup> In addition, an efficient method should at the same time take into account the constraints offered by arcs and multiple image systems, which are then likely to be present, as well as the weak lensing information. Again, this could be achieved by a maximum likelihood mass reconstruction.

It was noted for example by Kassiola, Kovner & Fort (1993), Wallington, Kochanek & Koo (1995), Colley, Tyson & Turner (1996) or Kneib et al. (1996), that it is necessary to include the effects of individual cluster galaxies in order to explain the details of the strong lensing features. By exploiting the morphology of strongly distorted images it might well be possible to set constraints on the mass distri-

<sup>‡</sup> In the likelihood method of Natarajan and Kneib (1997) a description of the 'cluster mass distribution' was assumed to be available *a priori* from the modelling of strong lensing features. In their simulations the mass models for the cluster galaxies were added to the same known cluster mass distribution for generating the data as well as for the analysis.

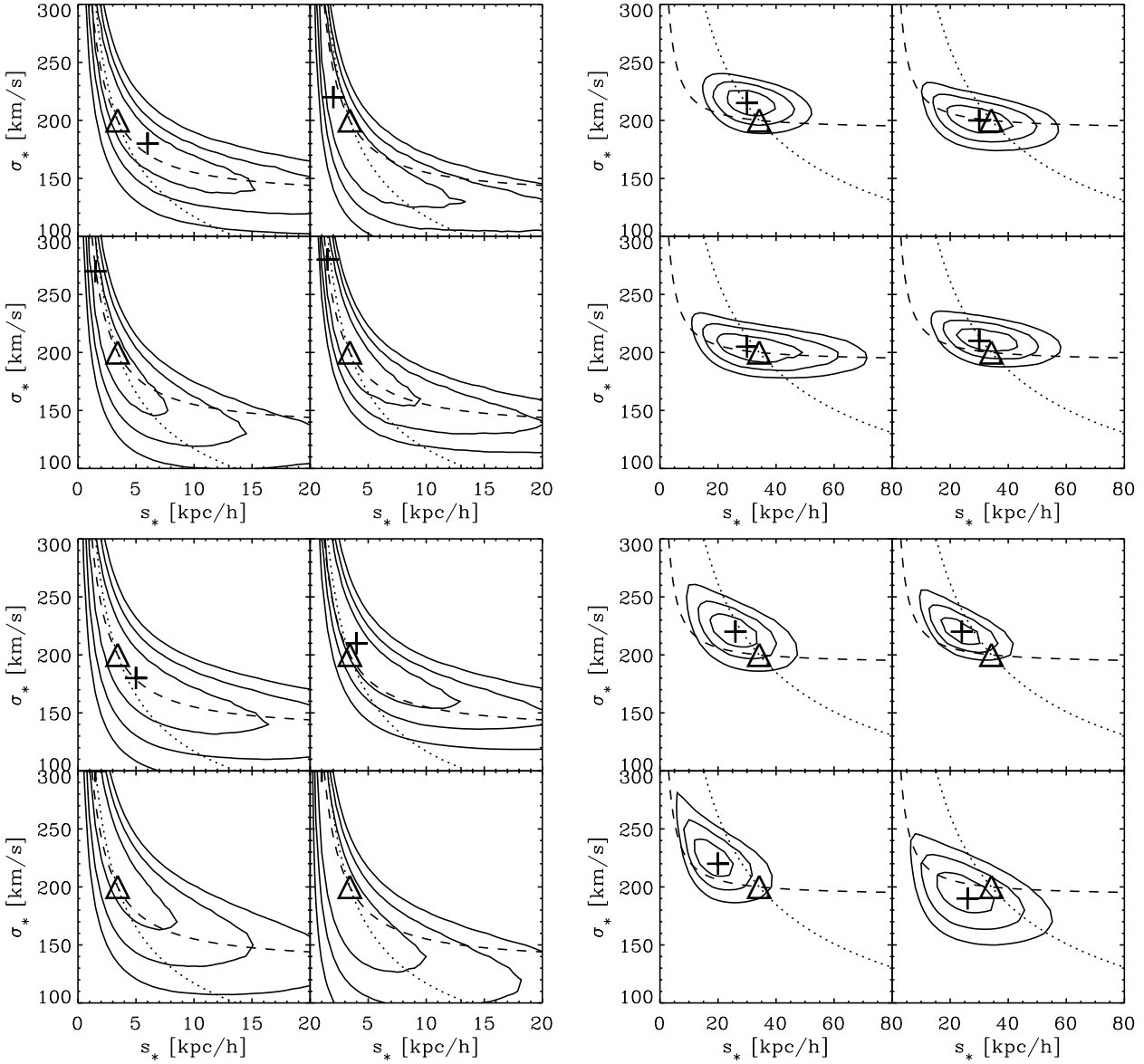


**Figure 7.** Confidence regions for the velocity dispersion and the cutoff radius for different random realizations. The sets of plots on the left are for the galaxy input model with a cutoff radius of  $s_* = 3.4 h^{-1}$  kpc, and those on the right for  $s_* = 34 h^{-1}$  kpc. Note their difference in the range of parameter values on the  $s_*$ -axis. As specified in the text, the top plots display the results including information provided by background galaxy images located in the outskirts of the cluster and the bottom plots are for the central region. The confidence contours are 99.73%, 95.4%, and 68.3%, determined in the way explained in Section 4.3 (without prior information), and the meaning of the lines and symbols is the same as in Fig. 6. The random realizations of cluster and background galaxies are the same as those used for Fig. 4.

bution of individual cluster galaxies which are located close to critical lines. First steps in this direction were made by Kassiola et al. (1993) and Wallington et al. (1995) for two bright cluster galaxies perturbing the arc system in the cluster 0024+1654.

#### 4.5 Scaling Parameters

For calculating the confidence regions shown in Figs. 6 and 7 we fixed the scaling parameters for the galaxy haloes at their input values ( $\eta = 4$ ,  $\nu = 0.5$ ). A comprehensive analysis within the mass model specified for this method should in

principle include a maximization of the likelihood over these *a priori* unknown parameters. This leads to a slight widening of the confidence regions, but it does not change any of the general conclusions drawn above.

Here the prospects for determining these scaling indices from the lensing analysis are briefly mentioned. Fig. 8 displays the confidence contours as a function of  $\eta$  and  $\sigma_*$ , and  $\nu$  and  $s_*$ . Each time the two remaining parameters were fixed at their input values. The plots reveal that the constraints on the velocity dispersion scaling index  $\eta$  are not particularly tight if the cutoff radius is small. In order to improve them it would be necessary to add the information

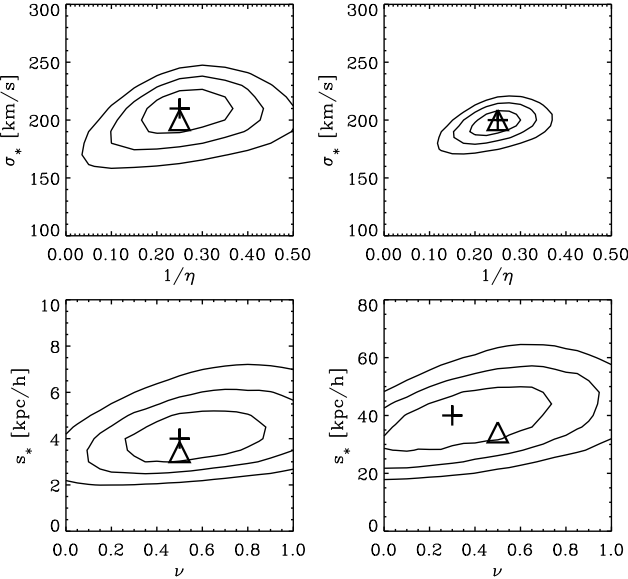


**Figure 8.** Confidence regions for the scaling parameters  $\eta$  and  $\nu$ . The **left** plots are for the galaxy input model with  $s_*$  =  $3.4h^{-1}$  kpc, taking into account the information from the total field of view. The **right** plots are for the extended halo model ( $s_*$  =  $34h^{-1}$  kpc) and only include the information provided by the background galaxy images located in the outskirts of the cluster as specified earlier in the text. The significance of the contours and the meaning of the symbols is analogous to the previous figures, and the random realization of cluster and background galaxies is the same as for the top right plot in each of the panels of Fig. 7.

from several galaxy clusters. In the case of extended dark matter haloes, however, the information available from one cluster is already sufficient to derive interesting limits on  $\eta$ , although we excluded the central data region of our simulations in this case in order to avoid the problems discussed in the previous section. Whereas the scaling prescription for the velocity dispersion can be motivated by observations as well as by physical arguments, the scaling law for the cutoff radius adopted for our analysis is rather hypothetical. In realistic applications within galaxy clusters one would expect a much stronger dependence of the galaxy halo extent on external effects rather than on the luminosity of the cluster galaxy, but apart from binning the data into subsets we did not investigate more quantitative methods for establishing such dependencies. The results on the scaling parameter  $\nu$  shown in the figure should therefore merely be regarded as an indication of the amount of information available.

#### 4.6 Potential Problems

A general problem for weak lensing studies is the degeneracy between the distance of the lensed source galaxies and the physical surface mass density – and hence the mass – of the lens. The quantity which is of importance in this context is the average  $\langle w \rangle_z$  of the relative lensing strength, which depends on the redshift distribution of the source galaxies (for a given cluster redshift and cosmology). In order to demonstrate the implications of incorrect assumptions on  $p_z(z)$ , we repeated the analysis for one of the diagrams shown earlier.

The confidence regions displayed in Fig. 9 were calculated for redshift distributions with  $\langle z \rangle = 0.5$  and  $\langle w \rangle_z = 0.55$ , and  $\langle z \rangle = 2$  and  $\langle w \rangle_z = 0.84$ , respectively, whereas the true distribution used for generating the data has  $\langle z \rangle = 1$  and  $\langle w \rangle_z = 0.75$ . The results confirm that an underestimate of  $\langle w \rangle_z$  leads to an overestimate of the velocity dispersion, and overestimating  $\langle w \rangle_z$  causes a displacement of the confidence contours towards smaller velocity dispersions. Note also that for the low cluster redshift of  $z_d = 0.16$ , large overestimates of the average source redshift  $\langle z \rangle$  do not strongly affect the results, because the relative lensing strength reaches an asymptotic value for increasing source redshift. The problem is more severe for higher-redshift clusters, and in principle specifying the parameter  $\sigma_*$  by other means allows to constrain the quantity  $\langle w \rangle_z$ . (This is true if the confidence contours are not ‘intrinsically’ extended in the  $\sigma_*$ -direction as it is the case for the low cutoff radius model.) As long as the lens is non-critical for all redshifts, the results do not strongly depend on higher moments of the redshift distribution, and any reasonably smooth function for  $p_z(z)$  should be adequate to approximate the correct description of the probability density distributions for image ellipticities (see Fig. 5). In the critical case, however, the image distortions carry a large amount of information on the redshift distribution of the sources, and then the sensitivity of the results to the choice of  $p_z(z)$  has to be taken more seriously.

The additional degeneracy expressed by the mass sheet transformation mentioned in Section 2.3 is present even if the average lensing strength is known. Although this degeneracy can be broken by other means, we would like to remark here that a transformation of the total mass distribution (including the galaxies) according to equation (11) merely implies a rescaling of the galaxy mass distributions. Therefore this leads to a shift of the confidence regions along the velocity dispersion coordinate, and it does not affect the conclusions on the radial extent of the dark matter haloes.

A potentially serious observational problem for the study described in this paper could be the reliable identification of cluster galaxies. We tested the importance of this issue by ignoring faint cluster galaxies during the likelihood analysis. For the respective diagrams of Fig. 9 we took into account cluster galaxies brighter than  $0.3 L_*$  (129 galaxies) or brighter than  $L_*$  (34 galaxies), whereas the calculation of the image shapes of background galaxies included 259 cluster galaxies brighter than  $0.1 L_*$  within the analysis region for this particular realization. The results demonstrate that despite their large numbers, the contribution of very faint cluster members to the lensing signal is only marginal. The information contributed by cluster galaxies between  $0.3 L_*$  and  $L_*$ , and those brighter than  $L_*$  is comparable, because the smaller numbers of bright and massive galaxies are compensated by their stronger distortion effects. Neglecting the presence of fainter cluster members only increases the noise level and does not systematically affect the results. This also indicates that possible small scale clumps in the dark matter distribution which are not associated to luminous galaxies do not bias the results of the likelihood analysis.

Finally, in applications to real observations a distinction could be made between spiral and elliptical cluster galaxies because they require different normalizations for the velocity dispersion parameter. This can be done iteratively, searching for the best solution for one kind of galaxies at a time, and

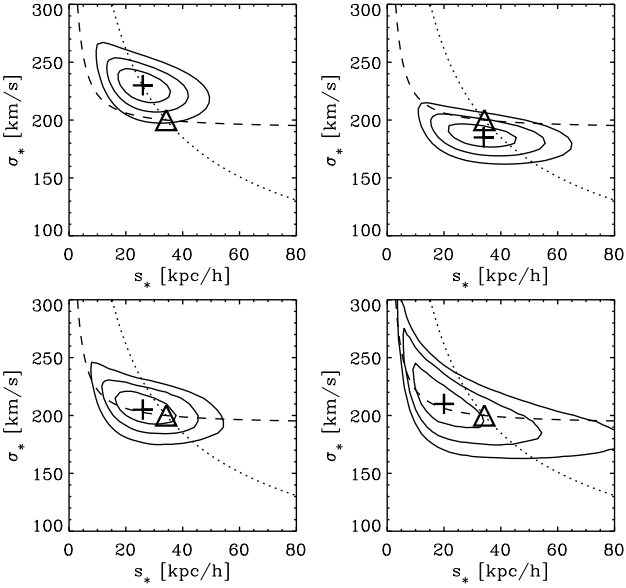


**Figure 9.** The consequences of potential problems. These diagrams should be compared with the top right plot in the top right panel of Fig. 7. The **top** plots demonstrate the effects of assuming an incorrect redshift distribution for the source galaxies. The **left** plot is for a distribution according to equation (10) with  $\langle z \rangle = 0.5$  and  $\beta = 1$ , and the **right** one for  $\langle z \rangle = 2$  and  $\beta = 1$ . In the **bottom** plots the analysis only includes cluster galaxies brighter than  $0.3 L_*$  (**left**), or brighter than  $L_*$  (**right**). The significance of the contours and the meaning of the symbols is analogous to the previous figures.

should not cause additional problems. However, due to the dominance of early-type galaxies, this distinction may be unnecessary in many clusters.

## 5 DISCUSSION

We investigated methods to constrain the mass distribution of cluster galaxies from the distortions of the images of faint background galaxies. In this paper we restricted the treatment to non-critical clusters (or the non-critical regions of critical ones), and we did not discuss the observational difficulties in measuring image ellipticities or identifying cluster galaxies.

The  $\zeta$ -statistic is a straightforward method for determining aperture masses. Significant (aperture) mass estimates for an ensemble of cluster galaxies can be obtained by adding the results for a large number of galaxies. The method provides a direct handle on the lensing signal of the cluster galaxies without the need to specify a model for their mass distribution. The galaxy lensing effects are amplified by an underlying cluster mass distribution. Hence, in regions with non-negligible surface mass density, a cluster mass reconstruction is necessary in order to take this effect into account in the calculation of the  $\zeta$ -statistic. Due to geometrical limitations it is not possible to include all available information into the method. Towards the cluster centre the increasing number density of cluster galaxies precludes a useful application of the  $\zeta$ -statistic. In addition, the generalization into the non-linear regime also implies an

increasing sensitivity to uncertainties in the description of the cluster mass distribution or the redshift distribution of the source galaxies. In the outskirts of clusters, however, the  $\zeta$ -statistic is applicable without major technical difficulties.

For a quantitative analysis, a maximum likelihood method is more appropriate. We tried to separate the treatment of cluster galaxies and a ‘global cluster mass distribution’ by reconstructing the latter one using standard inversion methods and then adding parametrized mass models for the galaxies on top of that. The results of our simulations demonstrate that this method is reliable – in the sense of correctly retrieving the input parameters for the galaxy mass models within their confidence regions – as long as the mass in galaxies is small compared to the total mass of the system. However, if the cluster galaxies do have extended dark matter haloes, this is not the case. The potentially significant mass fraction contributed by them also shows up in the cluster mass reconstruction, and adding additional mass in the form of galaxy models would violate the total mass constraint given by the reconstruction. We dealt with that problem by applying empirical and admittedly inelegant mass compensation procedures. This approach turned out to be workable, though not completely satisfying, in the outskirts of clusters where the requirements on the accuracy of the description of the cluster mass component are moderate.

In the highly non-linear region of the cluster centre, however, it is impossible to treat the image distortion effects caused by a global mass component and those caused by individual cluster galaxies independently. Rather, the principle of maximum likelihood should be taken seriously and the method of choice should allow to determine the best description of the cluster mass component for each given set of galaxy model parameters by explicitly taking the presence of the galaxies into account. In general, this cannot be accomplished by resorting to simple parametrized mass models for the cluster component itself. These represent an unjustified restriction and could therefore severely bias the results. Observational as well as numerical work indicates that clusters of galaxies cannot be regarded as nicely virialized systems. Instead, their mass distribution often exhibits complicated morphologies and hence a virtually parameter-free approach is warranted for describing them. We developed a generalized maximum likelihood method which enables us to cope with the problems discussed above and we will report on our experience therewith elsewhere.

In those cases for which we classified the likelihood method presented in this paper as reliable or applicable, we believe that the general picture provided by the confidence regions in the galaxy model parameter space is correct. Nevertheless, introducing additional degrees of freedom by allowing the cluster component to adapt to changes of the galaxy model will tend to widen the confidence regions. Especially for the galaxy input model with extended dark matter haloes an even more pronounced elongation of the confidence regions along the cutoff radius coordinate in the model parameter space can be expected. In a reliable analysis for extended galaxy haloes in the central cluster region, this should then be the case as well. This model degeneracy between mass in galaxies and mass in a global cluster component also reflects the conceptual difficulties of making a clear-cut distinction between the two. Without further in-

formation on the dynamical state of this matter, it might be more appropriate to interpret the results on the cutoff radius of galaxies near the cluster centre as a characteristic scale of mass clumping around cluster galaxies rather than necessarily as ‘the extent of the galaxy mass distribution’.

In our simulations we specified two extreme models for the cutoff radius of cluster galaxies, and in the discussion we concentrated on investigating the capabilities of reliably retrieving these well-defined input values for the mass model parameters. Although it is difficult to tightly constrain ‘the extent of the dark matter haloes’ from the information available, it is nevertheless feasible to distinguish with high significance between extreme models with or without extended dark matter halo, as well as to detect possible spatial variations of the galaxy halo properties. In realistic situations, a dependence on the physical distance from the cluster centre or the (three-dimensional) density of the environment could be expected, whereas the observations only allow direct access to the projected distance and the surface mass density. For example, if the extent of the galaxy halo is determined by the density of the environment, a linear dependence of the cutoff radius on the physical distance from the cluster centre could be expected for clusters with isothermal mass profile. In more sophisticated simulations a dependence of the cutoff radius as a function of the density of the environment or the distance from the cluster centre could be explicitly included. This would allow to develop effective strategies for quantifying possible trends of the characteristic extent of galaxy haloes and to assess the uncertainties introduced by projection effects. For a more direct comparison of observable effects with theoretical predictions, another option is to use high resolution N-body simulations in which cluster galaxies can be resolved individually.

Although the analysis in this paper was confined to a single cluster, the results from different clusters can easily be combined statistically. The observational prospects of weak lensing studies have been widely discussed in recent years, and several observations which are suitable for carrying out the kind of project described here are already available.

Shortly before the submission of this paper, a preprint was put on the web by Natarajan et al. (1997). They applied the methods of Natarajan & Kneib (1997) to HST images of the cluster AC114, detected a galaxy-galaxy lensing signal, and obtained an estimate of  $\approx 10h^{-1}$  kpc for the size of an  $L_*$ -galaxy halo. When compared to the results of Brainerd et al. (1996) this provides an indication that the haloes of cluster galaxies are less extended than those of field galaxies.

## ACKNOWLEDGMENTS

We thank Matthias Bartelmann for making the N-body cluster simulation available, Stella Seitz for discussions, and Simon White for comments on the manuscript. This work was supported in part by the Deutscher Akademischer Austauschdienst (Doktorandenstipendium HSP III) and the Sonderforschungsbereich 375-95 der Deutschen Forschungsgemeinschaft.

## REFERENCES

Bartelmann M., Steinmetz M., Weiss A., 1995, A&A, 297, 1  
 Bartelmann M., Narayan R., 1995, ApJ, 451, 60  
 Bartelmann M., Narayan R., Seitz S., Schneider P., 1996, ApJ, 464, L115  
 Brainerd T.G., Blandford R.D., Smail I., 1996, ApJ, 466, 623  
 Broadhurst T.J., Taylor A.N., Peacock J.A., 1995, ApJ, 438, 49  
 Colley W.N., Tyson J.A., Turner E.L., 1996, ApJ, 461, L83  
 Fahlman G., Kaiser N., Squires G., Woods D., 1994, ApJ, 437, 56  
 Falco E.E., Gorenstein M.V., Shapiro I.I., 1985, ApJ, 289, L1  
 Fischer P., Bernstein G., Rhee G., Tyson J.A., 1997, AJ, 113, 521  
 Griffiths R.E., Casertano S., Im M., Ratnatunga K.U., 1996, MNRAS, 282, 1159  
 Kaiser N., 1995, ApJ, 439, L1  
 Kaiser N., Squires G., 1993, ApJ, 404, 441  
 Kassiola A., Kovner I., Fort B., 1993, ApJ, 400, 41  
 Kneib J.-P., Ellis R.S., Smail I., Couch W.J., Sharples R.M., 1996, ApJ, 471, 643  
 Maoz D., Rix H.-W., 1993, ApJ, 416, 425  
 Natarajan P., Kneib J.-P., 1997, MNRAS, 287, 833  
 Natarajan P., Kneib J.-P., Smail I., Ellis R.S., 1997, preprint, astro-ph/9706129  
 Schneider P., Rix H.-W., 1997, ApJ, 474, 25  
 Schneider P., Seitz C., 1995, A&A, 294, 411  
 Schramm T., Kayser R., 1995, A&A, 299, 1  
 Seitz C., Schneider P., 1995, A&A, 297, 287  
 Seitz C., Schneider P., 1997, A&A, 318, 687  
 Seitz C., Kneib J.-P., Schneider P., Seitz S., 1996, A&A, 314, 707  
 Seitz S., Schneider P., 1996, A&A, 305, 383  
 Squires G., Kaiser N., 1996, ApJ, 473, 73  
 Squires G., Kaiser N., Fahlman G., Babul A., Woods D., 1996, ApJ, 469, 73  
 Wallington S., Kochanek C.S., Koo D.C., 1995, ApJ, 441, 58  
 Zaritsky D., Smith R., Frenk C.S., White S.D.M., 1997, ApJ, 478, 53  
 Zaritsky D., White S.D.M., 1994, ApJ, 435, 599